Application of LES Technique to Diagnosis of Wind Farm by Using High Resolution Elevation Data*

Takanori UCHIDA** and Yuji OHYA**

We are developing the numerical model called the RIAM-COMPACT (Research Institute for Applied Mechanics, Kyushu University, Computational Prediction of Airflow over Complex Terrain). The object domain of this numerical model is from several m to several km, and can predict the airflow and the gas diffusion over complex terrain with high precision. The RIAM-COMPACT has already been marketed by certain tie-up companies. The estimation of the annual electrical power output is also possible now based on the field observation data. In the present study, wind simulation of an actual wind farm was executed using the high resolution elevation data. As a result, an appropriate point and an inappropriate point for locating a wind turbine generator were shown based on the numerical results obtained. This cause was found to be a topographical irregularity in front of the wind turbine generator.

Key Words: Computational Fluid Dynamics, Unsteady Flow, Wind Mill, LES, Complex Terrain, High Resolution Elevation Data

1. Introduction

There exists a great and urgent need to reduce CO_2 emissions as a way to combat global warming. Therefore, attention has focused on the development of environmentally friendly wind energy (natural energy). In Japan, the number of wind power generation facilities has increased rapidly from several WTGs (Wind Turbine Generators) to a large-scale WF (Wind Farm). The output of the WTG is proportional to the cube of the wind speed. Therefore, it is important that the windy region in which the WTG is installed be chosen carefully. The terrain in Japan is remarkably different from that of Europe and America, and thus it is extremely important to consider Japan's unique topographic effect on the wind, such as a local speed-up, separation, reattachment, and so on.

The social and technological requirements for wind power are strong. Concentrating on a space of several km or less, we are developing an unsteady, non-linear-type numerical simulator called the RIAM-COMPACT (Research Institute for Applied Mechanics, Kyushu University, Computational Prediction of Airflow over Complex Terrain)[1]–[3]. The RIAM-COMPACT is a FORTRAN program based on the FDM (Finite-Difference Method), and adopts an LES (Large-Eddy Simulation) technique as a turbulence model. In an LES, comparatively large eddy structures are calculated directly, and only eddy structures that are smaller than the calculation mesh are modeled.

Up to now, most of the software that has been developed in Japan employs the time-averaged turbulence model called the RANS (Reynolds Averaged Navier-Stokes equation) from the problem regarding the necessary time required for calculation[4],[5]. Computer performance has improved remarkably in recent years, and the problem regarding calculation time has been reduced dramatically. LES, a turbulence model of the space-average type, can simulate an unsteady flow field. If an unsteady flow field can be easily calculated, and the result reproduced in animation, the RIAM-COMPACT can provide an alternative tool for wind tunnel experiment. Consequently, it is expected to aid in practical design. We have been examining the practical use of the RIAM-COMPACT for several years from such a viewpoint. The RIAM-COMPACT has already been marketed by certain tie-up companies. Estimation of annual electrical power output is also possible now based on field observation data.

The main problem regarding the current WF is its low power output. It is thought that the main cause of this inef-

* Received 24th March, 2006 (No. 06-4033)

** Research Institute for Applied Mechanics (RIAM), Kyushu University, 6–1 Kasuga-koen, Kasuga-city, Fukuoka 816–8580, Japan. E-mail: takanori@riam.kyushu-u.ac.jp

ficiency is due to small geographical rises and depressions in the WTG site. It has been assumed that these irregularities mechanically generate wind turbulence. Therefore, a regular evaluation of flow characteristics is necessary in the WF during operation. We thus propose the use of the RIAM-COMPACT to diagnose the WF site's airflow characteristics. The high resolution elevation data of 10 m or less that reflects the current state of land use is indispensable to this. We developed a technique for constructing high resolution elevation data of 10 m or less based on a paper map and the CAD (Computer Aided Design) data in DXF (Data eXchange Format) form[6]. In the present study, the numerical simulation for a WF during operation was executed by using elevation data of 5 m resolution.

2. The Characteristics of the RIAM-COMPACT

2.1 Governing equations

We consider a three-dimensional airflow of incompressible and viscous fluid over complex terrain with characteristic length scales on the order of kilometers, so that the Coriolis force can be neglected. In a DNS, the dimensional governing equations consist of the continuity and Navier-Stokes equations, as follows:

$$\frac{\partial u_i}{\partial x_i} = 0 \tag{1}$$

$$\frac{\partial u_i}{\partial t} + u_j \frac{\partial u_i}{\partial x_j} = -\frac{1}{\rho_0}\frac{\partial p}{\partial x_i} + \frac{\mu}{\rho_0}\frac{\partial^2 u_i}{\partial x_j \partial x_j} \tag{2}$$

where the subscripts i and $j = 1$, 2, and 3 correspond to the streamwise (x), spanwise (y), and vertical (z) directions, respectively. In the above equations, u_i is the instantaneous velocity component in the i-direction, p is the instantaneous pressure, ρ_0 is the reference density, and μ is the viscosity coefficient. All the variables are non-dimensionalized by an appropriate velocity U_{in} and a length scale h, such as $u_i^* = u_i/U_{\text{in}}$ and $x_i^* = x_i/h$, resulted in the following dimensionless equations:

$$\frac{\partial u_i}{\partial x_i} = 0 \tag{3}$$

$$\frac{\partial u_i}{\partial t} + u_j \frac{\partial u_i}{\partial x_j} = -\frac{\partial p}{\partial x_i} + \frac{1}{Re}\frac{\partial^2 u_i}{\partial x_j \partial x_j} \tag{4}$$

where Re $(= \rho_0 U_{\text{in}} h/\mu)$ is the Reynolds number, and the asterisk is omitted.

In an LES, the flow variables are divided into a GS (Grid-Scale) part and a SGS (SubGrid-Scale) part by the filtering operation. The filtered continuity and Navier-Stokes equations written in non-dimensional form are given by

$$\frac{\partial \bar{u}_i}{\partial x_i} = 0 \tag{5}$$

$$\frac{\partial \bar{u}_i}{\partial t} + \bar{u}_j \frac{\partial \bar{u}_i}{\partial x_j} = -\frac{\partial \bar{p}}{\partial x_i} - \frac{\partial \tau_{ij}}{\partial x_j} + \frac{1}{Re}\frac{\partial^2 \bar{u}_i}{\partial x_j \partial x_j} \tag{6}$$

where $\bar{u}_i$ is the instantaneous filtered velocity component in the i-direction, and $\bar{p}$ is the instantaneous filtered pressure. The effect of the unresolved subgrid-scales appears in the SGS stress as follows:

$$\tau_{ij} = \overline{u_i u_j} - \bar{u}_i \bar{u}_j \tag{7}$$

which must be modeled. In this study, τ_{ij} is parameterized by an eddy viscosity assumption of Smagorinsky[7] through the following constitutive relations:

$$\tau_{ij} - (\delta_{ij}/3)\tau_{kk} = -2\nu_{\text{SGS}}\bar{S}_{ij} \tag{8}$$

$$\nu_{\text{SGS}} = (C_s f_s \Delta)^2 |\bar{S}| \tag{9}$$

$$f_s = 1 - \exp(-z^+/25) \tag{10}$$

$$|\bar{S}| = (2\bar{S}_{ij}\bar{S}_{ij})^{1/2} \tag{11}$$

$$\bar{S}_{ij} = \frac{1}{2}\left(\frac{\partial \bar{u}_i}{\partial x_j} + \frac{\partial \bar{u}_j}{\partial x_i}\right) \tag{12}$$

$$\Delta = (h_x h_y h_z)^{1/3} \tag{13}$$

where δ_{ij} is the Kronecker delta, ν_{SGS} is the eddy viscosity, $\bar{S}_{ij}$ is the resolved strain-rate tensor, C_s $(= 0.1)$ is the dimensionless model coefficient (i.e., Smagorinsky constant), which is multiplied by the Van Driest exponential wall damping function f_s in order to account for the near wall effect, Δ is the grid-filter width, which is a characteristic length scale of the largest subgrid-scale eddies, and $|\bar{S}|$ is the magnitude of the resolved strain-rate tensor.

2.2 Coordinate system and variable arrangement

The most important factor involved in a successfully accurate simulation of airflow over complex terrain is correctly determining how to specify the topography model as the boundary conditions in the computation. For this purpose, we examine two coordinate systems and their corresponding variable arrangement. The first system involves a Cartesian non-uniform staggered grid, where the Cartesian velocity components are defined at the mid-point on their corresponding cell surfaces, whereas only the pressure is defined at the center of a cell. The other system is a generalized curvilinear collocated grid, where the Cartesian velocity components and pressure are defined at the center of a cell, while the volume flux components multiplied by the Jacobian are defined at the midpoint on their corresponding cell surfaces. In the case of a Cartesian non-uniform staggered grid, the rectangular grids represent the topography model imposed in the calculation. If we employ a Cartesian non-uniform staggered grid, then the original governing equations in the physical space are directly discretized without any coordinate transformation. On the other hand, if we employ a generalized curvilinear collocated grid, then the original governing equations in the physical space are transformed to the computational space through a coordinate transformation. As a result, the discretized governing equations based on a Cartesian non-uniform staggered grid become simpler than those based on a generalized curvilinear collocated grid. However, it should be noted here that both CFD codes show the same results in terms of CPU time and overall airflow characteristics over complex terrain[1].

2.3 Numerical method

The coupling algorithm of the velocity and pressure fields is based on a fractional step method[8] with the Euler explicit scheme. Therefore, the velocity and pressure fields are integrated by the following procedure. In the first step, the intermediate velocity field is calculated from the momentum equations without the contribution of the pressure gradient. In the next step, the pressure field is computed iteratively by solving the Poisson equation with the successive over relaxation (SOR) method. Finally, the divergence-free velocity at the $(n+1)$ time-step is then obtained by correcting the intermediate velocity field with the computed pressure gradient. As for the spatial discretization in the governing equations, a second-order accurate central difference approximation is used, except for the convective terms. For the convective terms written in non-conservation form, a modified third-order upwind biased scheme[9] is used. The weight of the numerical viscosity term is sufficiently small ($\alpha = 0.5$), compared to the Kawamura-Kuwahara scheme ($\alpha = 3$)[10].

3. Numerical Results and Discussion

In the present study, the numerical simulation for a WF during operation was executed by using a generalized curvilinear collocated grid. Only the calculation for the prevailing wind direction was done in this research. Moreover, the geographical features handled for this research is used as an arbitrary place.

Figure 1 shows the geographical features around the WTGs and numerical conditions. In the present study, the surroundings of the WTGs sites were constructed from CAD data of the DXF form with 5 m resolution. The surroundings were constructed with 50 m elevation data provided by the Geographical Survey Institute. Thus, the high resolution elevation data originally constructed based on the paper map and the DXF file were merged with existing elevation data by using the GIS (Geographical Information System) technique. The elevation data took several days to construct. The elevation data measured using a laser profiler, and free space shuttle elevation data (SRTM: Shuttle Radar Topography Mission data) is also used. In the RIAM-COMPACT, if the diameter of the rotor, the height of the hub, and the display color, etc. are set, and the location point is specified, the 3D line chart of the WTG can be inserted into the calculation result. The WTG in the present study has a rotor diameter of 52 m, and a hub height of 44 m. To clarify the topographic effect on the wind field near the ground, the surface roughness, such as a forest canopy, is not considered. The boundary conditions for the velocity field in the computational domain are as follows: 1/7 power law profile (inflow), free-slip condition (top and side boundary), convective outflow condition (outflow), non-slip condition (ground).

Figure 2 shows the instantaneous velocity vectors at

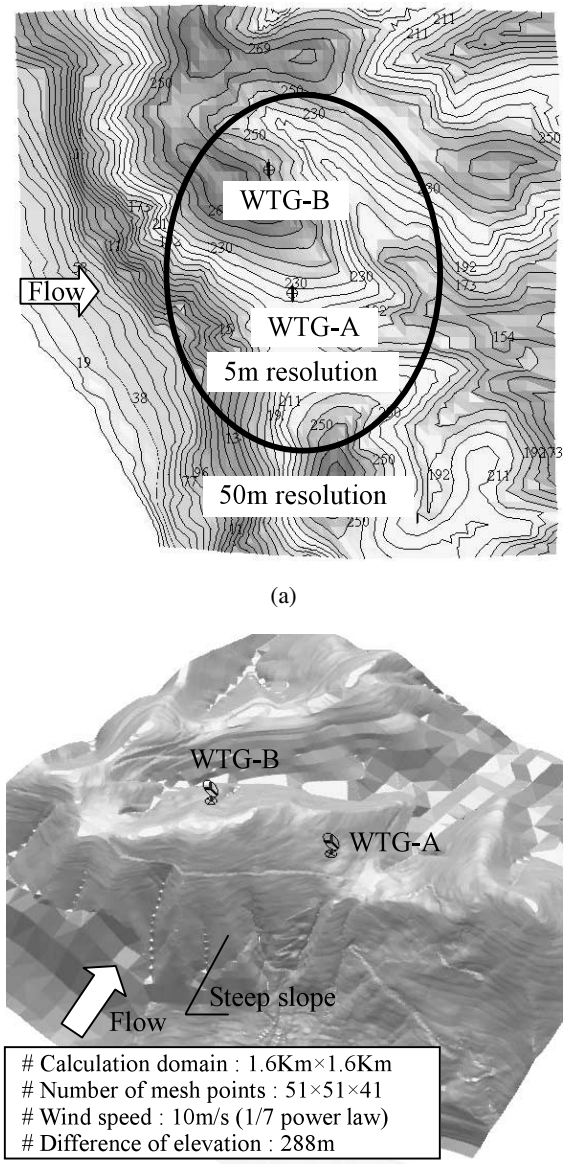

Fig. 1 Geographical features around WTGs: (a) Top view of contour lines of elevation data; (b) Bird's-eye view

the height of the hub ($z^* = 44$ m). The change in the vector is larger in WTG-B than in WTG-A. To clarify this difference, gust $|u'|$ $(=|u - U_{\mathrm{ave}}|)$ distributions corresponding to Fig. 2 are shown in Fig. 3. Here, u, u', and U_{ave} are dimensionless quantity on the same mesh point, and U_{ave} means the time-averaged wind speed. The contour chart displays values ranging from 0.05 to 0.5 by dividing into 30. It is understood that the contour of the gust $|u'|$ appears around WTG-B. It should be noted that the distribution of contour lines changed with time. This mechanism is described later. Such time variation can be simulated only by the unsteady turbulence model.

When the velocity vector and corresponding gust distributions in the vertical plane of each WTG are displayed,

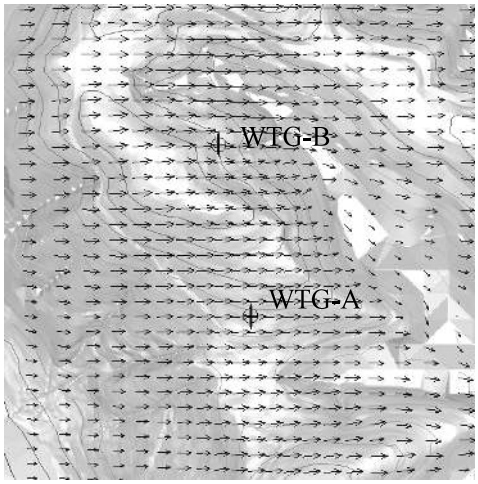

(a)

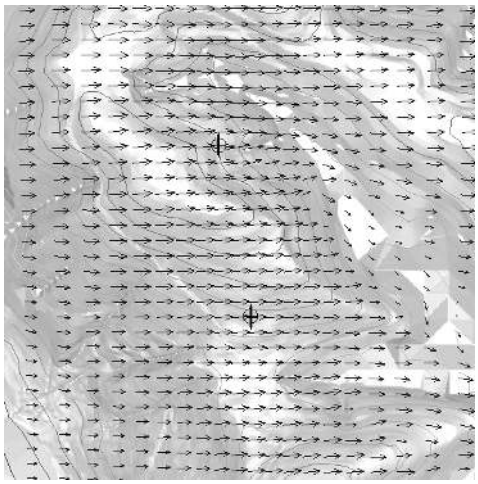

(b)

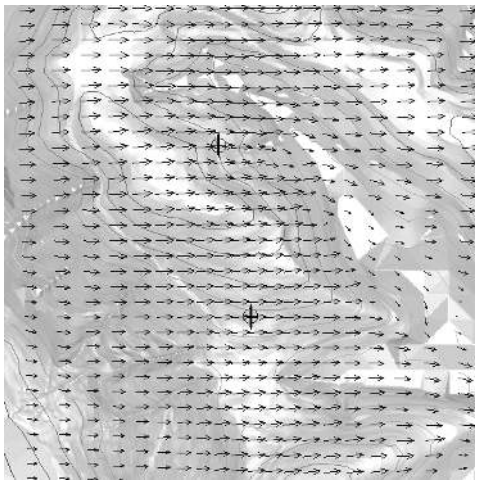

(c)

Fig. 2 Time evolution of velocity vectors at the height of the hub ($z^* = 44$ m): (a) Time = T_1; (b) Time = $T_1 + \Delta T$; (c) Time = $T_1 + 2\Delta T$

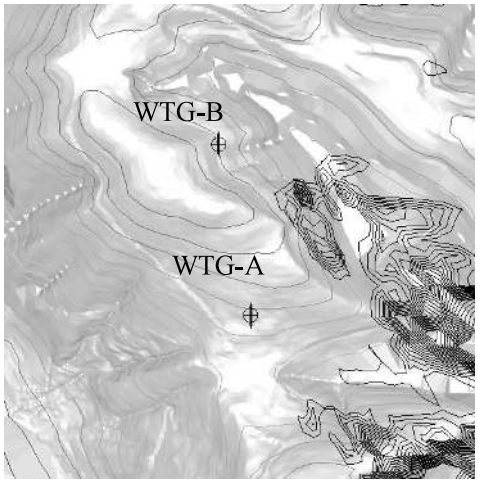

(a)

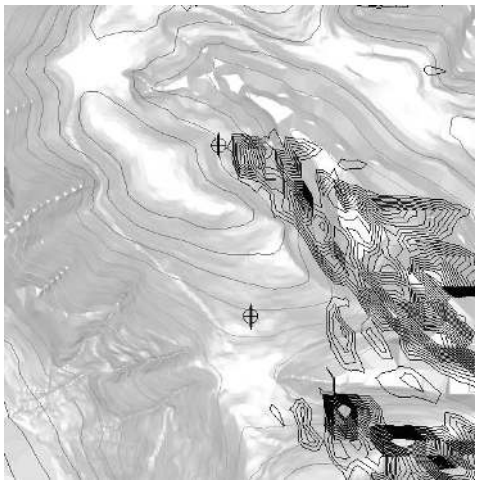

(b)

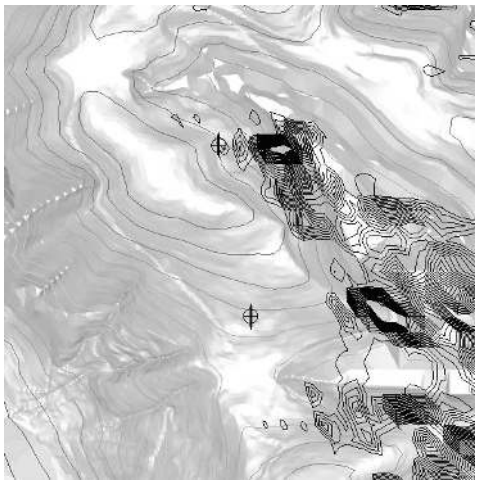

(c)

Fig. 3 Time evolution of gust components ($= |u - U_{\mathrm{ave}}|$) at the height of the hub ($z^* = 44$ m): (a) Time = T_1; (b) Time = $T_1 + \Delta T$; (c) Time = $T_1 + 2\Delta T$

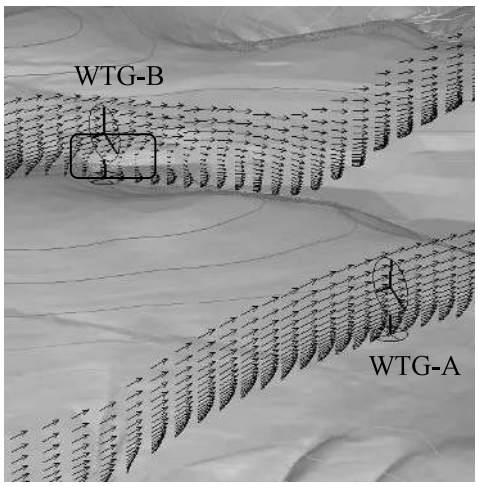

(a)

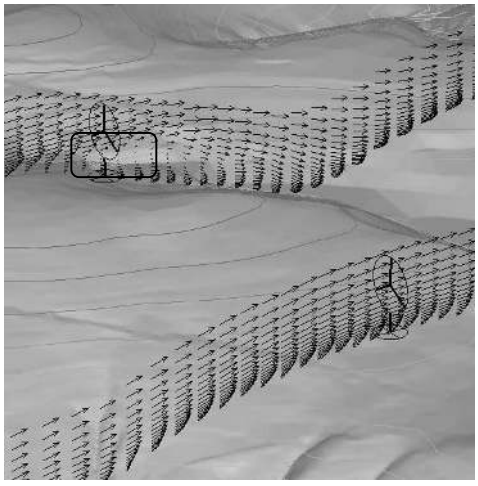

(b)

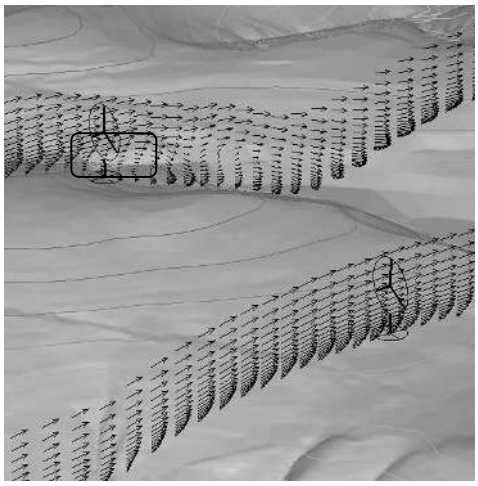

(c)

Fig. 4 Time evolution of velocity vectors in the vertical plane of each WTG: (a) Time = T_1; (b) Time = $T_1 + \Delta T$; (c) Time = $T_1 + 2\Delta T$

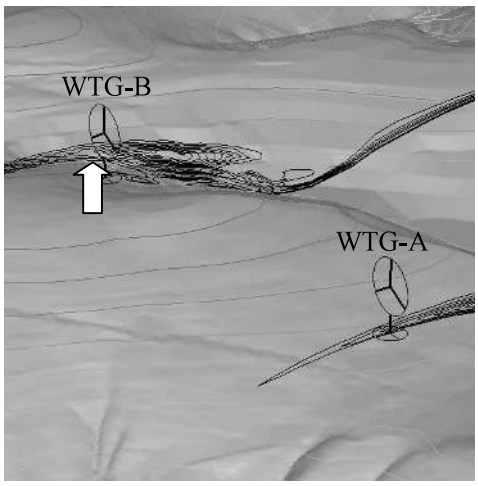

(a)

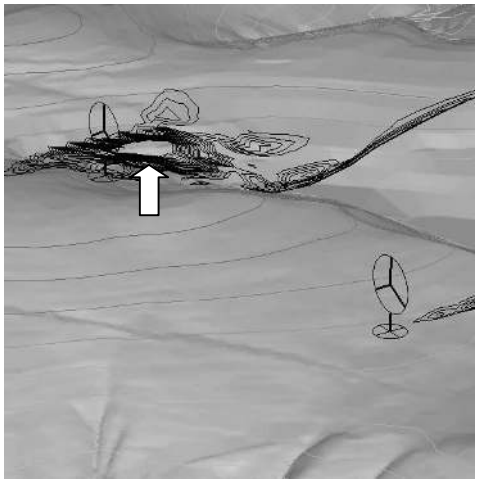

(b)

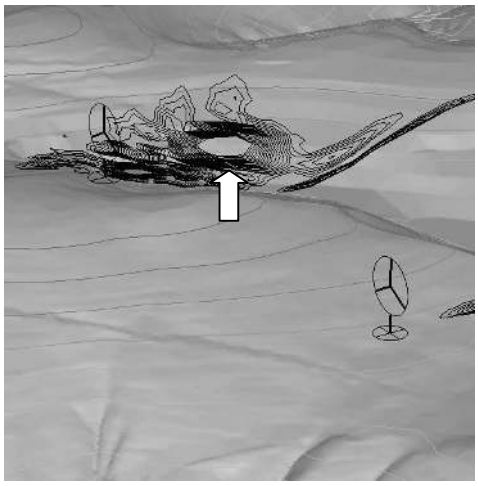

(c)

Fig. 5 Time evolution of gust components ($= |u - U_{ave}|$) in the vertical plane of each WTG: (a) Time = T_1; (b) Time = $T_1 + \Delta T$; (c) Time = $T_1 + 2\Delta T$

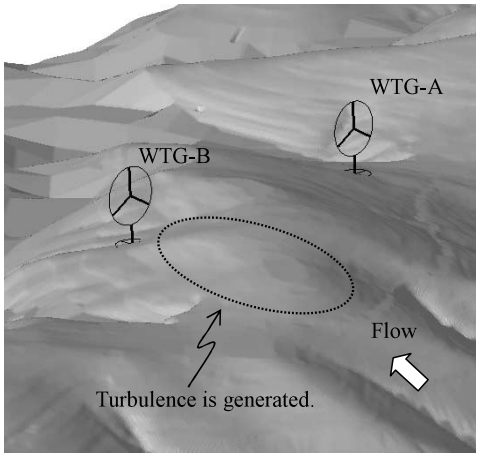

Fig. 6 Close-up of geographical features around WTGs

the difference of flow characteristics of both WTG-A and WTG-B becomes clearer. Figures 4 and 5 show the results. In the case of WTG-A, it is understood that all rotor heights share almost the same speed distribution. In addition, a local speed-up due to geographical effects is confirmed. On the other hand, the separated flow is confirmed under the rotor center in the case of WTG-B, shown by the solid line in Fig. 4. This is due to the turbulent flow mechanically generated from the topographical irregularity in front of WTG-B. That is, WTG-B is influenced by the turbulent flow generated by geographical features; this tower is located in a low point that shifts slightly from the hilltop. The flow phenomenon shown here cannot be reproduced if high resolution elevation data of 5 m resolution is not used. The area in which wind speed varies greatly with time is confirmed by Fig. 5 (see the arrow). If animation was made, and this was observed, it turned out to cause a similar phenomenon repeatedly. That is, a periodic vortex shedding was seen to be caused by the geographical irregularity in front of WTG-B (see Fig. 6).

Figure 7 shows the velocity vectors and the corresponding contour lines of turbulence intensities for a time-averaged field at the height of the hub. The contour chart displays values ranging from 0.05 to 0.5 by dividing into 30. It should be noted that the influence of the turbulent flow, observed near the WTG-B as has been described up to now, cannot be confirmed only by the results shown in Fig. 7 (a) (corresponding to the results of steady turbulence model). Therefore, a description of the corresponding turbulence intensities (Fig. 7 (b)) and distributions in the vertical plane shown in Fig. 8 becomes extremely important.

In the following, a more quantitative evaluation is performed. Figures 9 and 10 show the time history of gust component u' $(= u - U_{\mathrm{ave}})$ at the height of $z^* = 18$, 44, and 70 m. This is a physical quantity shown in Figs. 3 and 5. The time scale of a horizontal axis is a dimensionless value normalized by the inflow wind speed and the difference of elevation in the calculation domain. The place where the

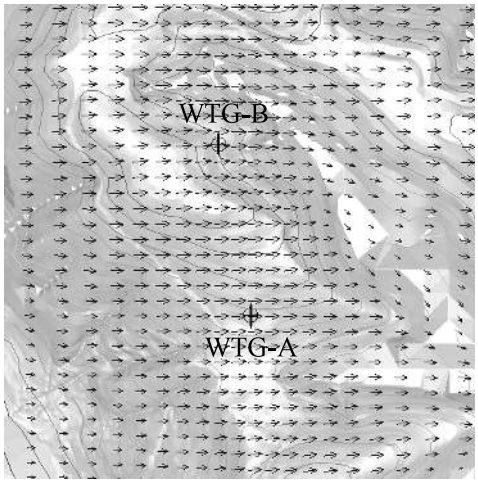

(a)

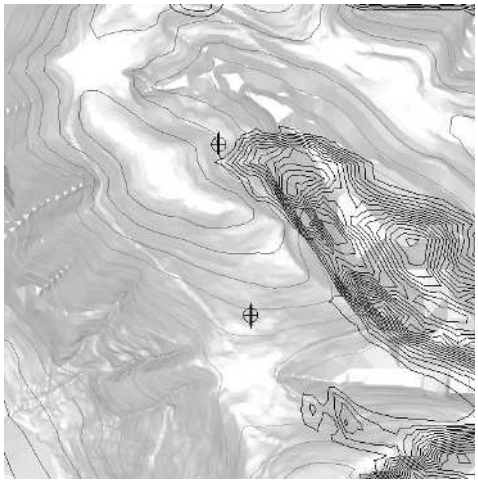

(b)

Fig. 7 Time-averaged field at the height of the hub ($z^* = 44$ m): (a) Velocity vectors; (b) Contour lines of turbulence intensities

time history was gathered is shown in these figures. In the case of WTG-A shown in Fig. 9, the gust component is zero at all height levels. That is, the influence of wind turbulence is extremely small. On the other hand, at the height of especially 18 m, sharp fluctuations are observed in the case of WTG-B shown in Fig. 10. This corresponds to the periodic vortex shedding described in Figs. 4 and 5.

Figures 11 and 12 show the vertical profiles of the sites of WTG-A and WTG-B. Figure 11 is a mean velocity profile. Figure 12 is a vertical profile of turbulence intensities. The vertical axis is a real scale distance from ground. The horizontal axis is a dimensionless value normalized by an inflow wind speed U_{in}. The rotor diameter is shown in the figure as well. In the case of WTG-A shown in Fig. 11 (a), it is understood to present almost the same speed distribution at all the height levels, as described in Fig. 4. In addition, a local speed-up by the effect of geographical features is confirmed at about 18 m height.

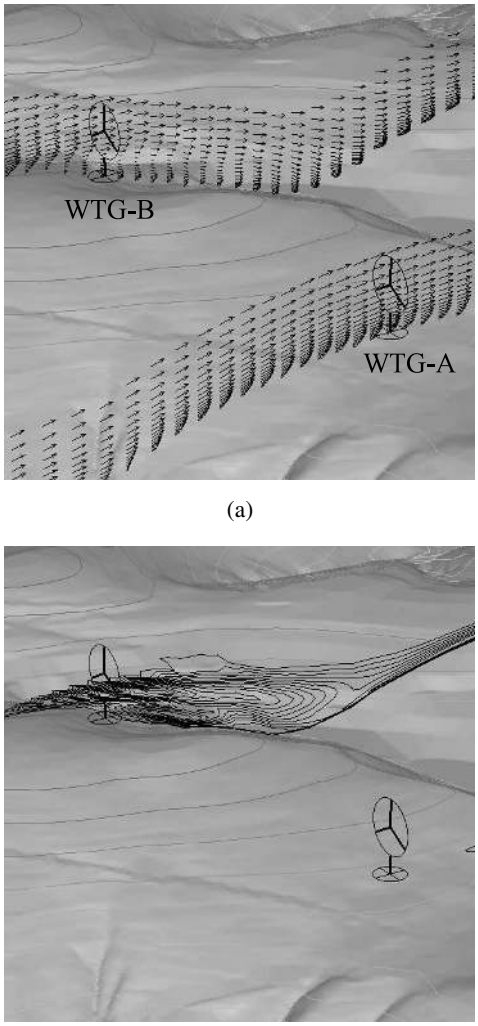

(a)

(b)

Fig. 8 Time-averaged field in the vertical plane of each WTG: (a) Velocity vectors; (b) Contour lines of turbulence intensities

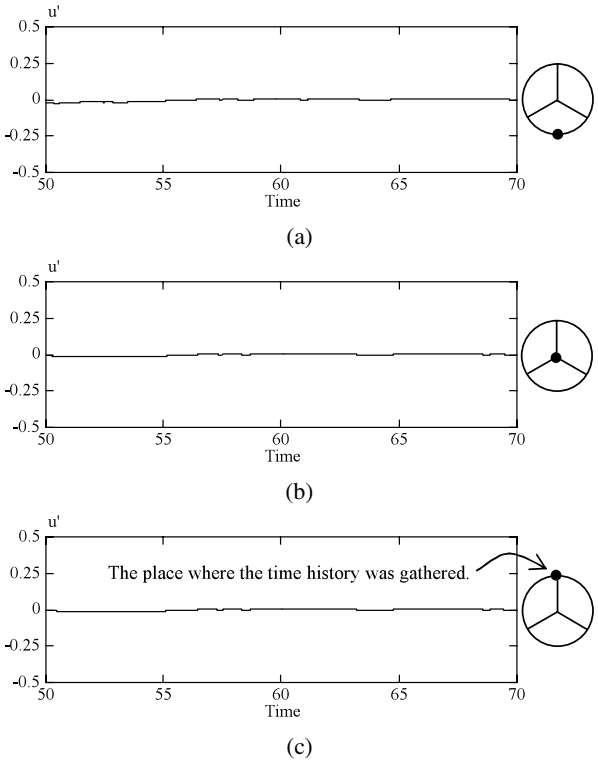

(a)

(b)

(c)

Fig. 9 Time history of u' of WTG-A: (a) $z^* = 18$ m; (b) $z^* = 44$ m (height of the hub center); (c) $z^* = 70$ m

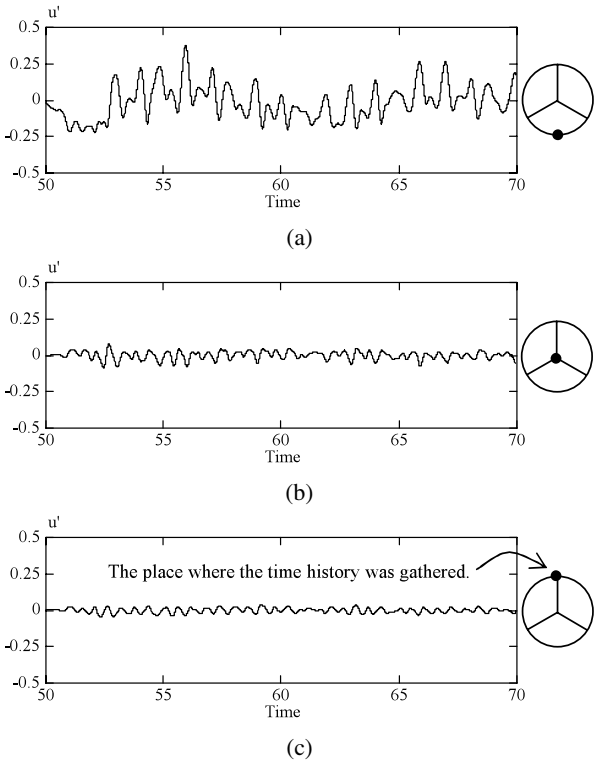

(a)

(b)

(c)

Fig. 10 Time history of u' of WTG-B: (a) $z^* = 18$ m; (b) $z^* = 44$ m (height of the hub center); (c) $z^* = 70$ m

In the case of WTG-B shown in Fig. 11 (b), a strong vertical wind shear is clearly seen. The result of showing in Fig. 11 is understood more clearly when examining a close-up of the velocity vectors for a time-averaged field in the vertical plane of each WTG, shown in Fig. 13.

The output power curve of WTG is provided for by the wind speed that flows in the hub's center without assuming the existence of the WTG. Additionally, a vertical wind shear based on a power law of about 1/5 or 1/7 is generally assumed. Therefore, it is expected that the amount of power generation will greatly fall below the calculation value when using earlier linear numerical model under a vertical wind shear that deviates greatly from the power law. It is thought that a strong vertical wind shear will become more important in association with the vibration or the fatigue strength of the tower used in WTG in the future. The values of the turbulence intensities of WTG-A shown in Fig. 12 (a) are very small at all heights. There-

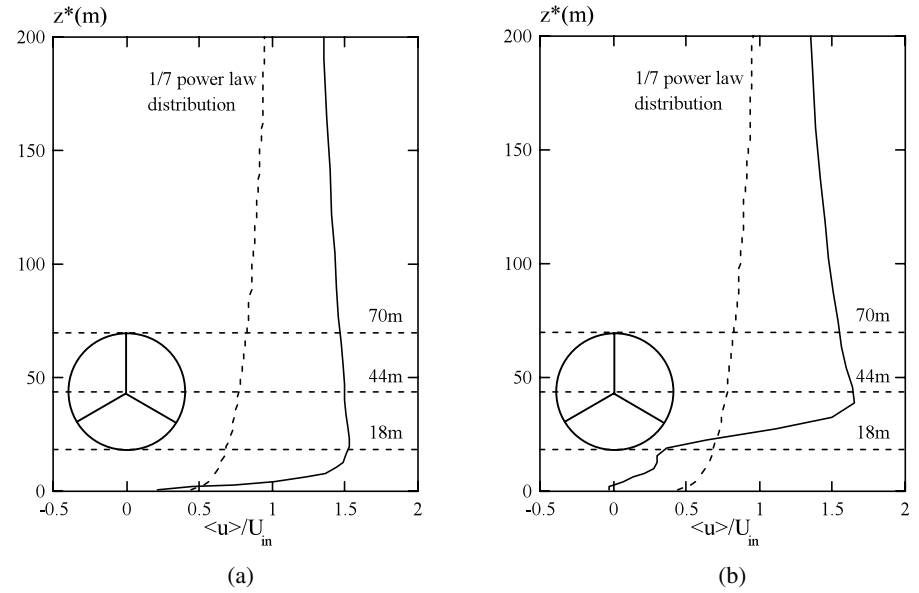

Fig. 11 Mean velocity profile: (a) WTG-A; (b) WTG-B

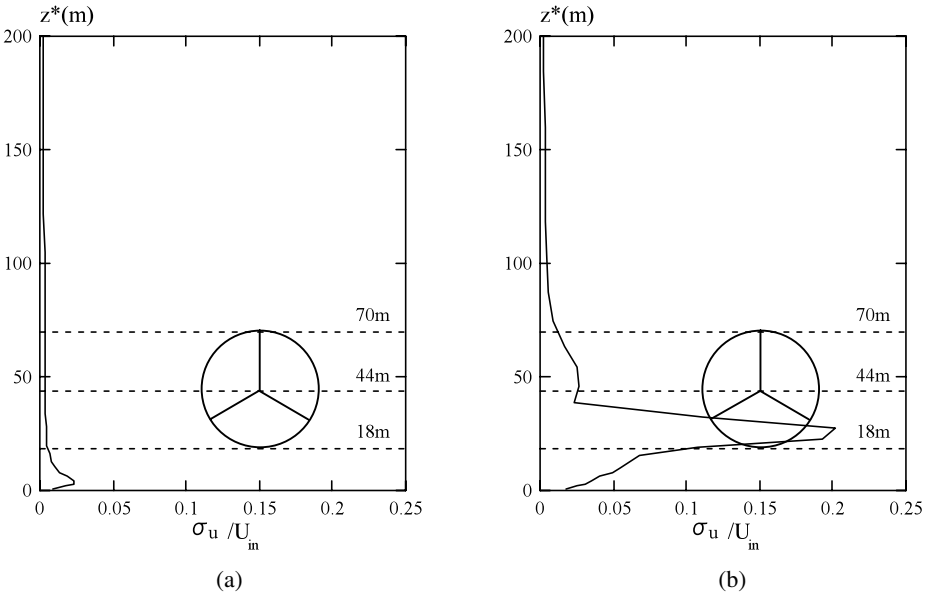

Fig. 12 Vertical profile of turbulence intensities: (a) WTG-A; (b) WTG-B

fore, it is understood that the wind turbulence caused by geographical irregularities hardly influences the electrical power output. On the other hand, the maximum value appears at about 20 m for WTG-B, as shown in Fig. 12 (b). This corresponds to the vicinity of the height where a strong vertical wind shear described in Fig. 11 (b) exists.

In this investigation, the influence of turbulence due to gustiness is not considered. It should be noted that only the turbulence mechanically or directly formed due to geographical irregularities is examined.

4. Concluding Remarks

In the present study, a numerical simulation for the WF during operation was executed by using elevation data of 5 m resolution. An appropriate point and an inappropriate point for locating a WTG were shown based on the numerical results obtained.

In the WF diagnosis for which careful investigation is needed, it was shown that both a detailed constructing of current land use and the simulation of unsteady winds were necessary. Moreover, past techniques that depend only on the wind speed distribution in the horizontal plane at the height of the hub were shown to be insufficient. It is necessary to display the gust component and the turbulence intensities as well as their vertical distributions. It is also important to graph these quantitatively at the same time. Especially, it is expected that the display of the wind speed's vertical distributions and the turbulence in-

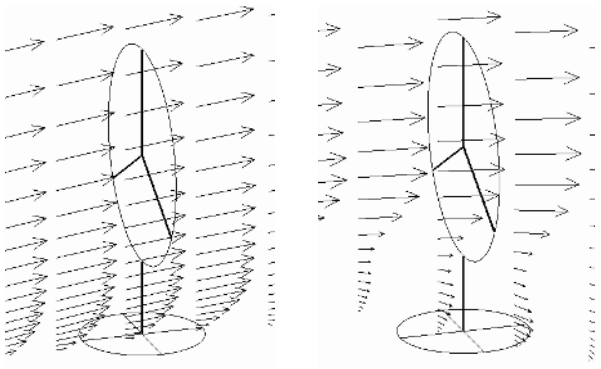

(a) (b)

Fig. 13 Close-up of velocity vectors for a time-averaged field in the vertical plane of each WTG: (a) WTG-A; (b) WTG-B

tensities will become more important as the use of WTG grows. It is necessary to examine the time variation of the wind speed that negatively influences the power generation output, using numerical simulations, wind tunnel experiments, and field observations. These are problems to be solved in the future. Consequently, the criteria for determining the most effective sites for WTG have been established, leading to the construction of location risk maps. This will greatly contribute to the establishment of suitable wind power generation in Japan.

Finally, it is predicted that the wind power generation facilities of the future will be established in relatively rugged places such as mountainous districts. Therefore, it is necessary that the sites of wind power generation facilities be examined with a high level of accuracy. It is thought that WF site planning that uses the high resolution altitude data of 10 m or less should be used in the preliminary investigation before the WTG is constructed.

References

(1) Uchida, T. and Ohya, Y., Numerical Simulation of Atmospheric Flow over Complex Terrain, J. Wind Eng. Ind. Aerodyn., Vol.81 (1999), pp.283–293.

(2) Uchida, T. and Ohya, Y., Large-Eddy Simulation of Turbulent Airflow over Complex Terrain, J. Wind Eng. Ind. Aerodyn., Vol.91 (2003), pp.219–229.

(3) Uchida, T. and Ohya, Y., Development of the Local Wind Field Simulator RIAM-COMPACT—Wind Field Assessment and Real Time Simulation—, J. Japan Society of Fluid Dynamics, (in Japanese), Vol.22, No.5 (2003), pp.417–428.

(4) Murakami, S., Mochida, A., Kato, S. and Kimura, A., Development and Verification of Local Area Wind Energy Prediction System LAWEPS, J. Japan Society of Fluid Dynamics, (in Japanese), Vol.22, No.5 (2003), pp.375–386.

(5) Ishihara, I., A Nonlinear Wind Prediction Model MASCOT : Development and Application, J. Japan Society of Fluid Dynamics, (in Japanese), Vol.22, No.5 (2003), pp.387–396.

(6) Uchida, T., Ohya, Y., Araya, R., Tanabe, M. and Kawashima, Y., Construction of High Resolution Elevation Data from Paper Map for Numerical Model "RIAM-COMPACT", Reports of Research Institute for Applied Mechanics, Kyushu University, (in Japanese), Vol.129 (2005), pp.135–141.

(7) Smagorinsky, J., General Circulation Experiments with the Primitive Equations, Part 1, Basic Experiments, Mon. Weather Rev., Vol.91 (1963), pp.99–164.

(8) Kim, J. and Moin, P., Application of a Fractional-Step Method to Incompressible Navier-Stokes Equations, J. Comput. Phys., Vol.59 (1985), pp.308–323.

(9) Kajishima, T., Upstream-Shifted Interpolation Method for Numerical Simulation of Incompressible Flows, Bull. Japan Soc. Mec. Eng. B, (in Japanese), Vol.60, No.578 (1994), pp.3319–3326.

(10) Kawamura, T., Takami, H. and Kuwahara, K., Computation of High Reynolds Number Flow around a Circular Cylinder with Surface Roughness, Fluid Dyn. Res., Vol.1 (1986), pp.145–162.